Numerical modeling of the propagation environment in the atmospheric boundary layer over the Persian Gulf

Numerical Modeling of the Propagation Environment in the Atmospheric Boundary Layer over the Persian Gulf

B. W. ATKINSON, J.-G. LI, AND R. S. PLANT

Department of Geography, Queen Mary and Westfield College, University of London, London, United Kingdom

(Manuscript received 8 November 1999, in final form 15 July 2000)

ABSTRACT

Strong vertical gradients at the top of the atmospheric boundary layer affect the propagation of electromagnetic waves and can produce radar ducts. A three-dimensional, time-dependent, nonhydrostatic numerical model was used to simulate the propagation environment in the atmosphere over the Persian Gulf when aircraft observations of ducting had been made. A division of the observations into high- and low-wind cases was used as a framework for the simulations. Three sets of simulations were conducted with initial conditions of varying degrees of idealization and were compared with the observations taken in the Ship Antisubmarine Warfare Readiness/Effectiveness Measuring (SHAREM-115) program. The best results occurred with the initialization based on a sounding taken over the coast modified by the inclusion of data on low-level atmospheric conditions over the Gulf waters. The development of moist, cool, stable marine internal boundary layers (MIBL) in air flowing from land over the waters of the Gulf was simulated. The MIBLs were capped by temperature inversions and associated lapses of humidity and refractivity. The low-wind MIBL was shallower and the gradients at its top were sharper than in the high-wind case, in agreement with the observations. Because it is also forced by land–sea contrasts, a sea-breeze circulation frequently occurs in association with the MIBL. The size, location, and internal structure of the sea-breeze circulation were realistically simulated. The gradients of temperature and humidity that bound the MIBL cause perturbations in the refractivity distribution that, in turn, lead to trapping layers and ducts. The existence, location, and surface character of the ducts were well captured. Horizontal variations in duct characteristics due to the sea-breeze circulation were also evident. The simulations successfully distinguished between high- and low-wind occasions, a notable feature of the SHAREM-115 observations. The modeled magnitudes of duct depth and strength, although leaving scope for improvement, were most encouraging.

1. Introduction

Radar wave propagation depends strongly on local meteorological conditions, especially in the atmospheric boundary layer (ABL), largely because of variations in the refractive index n. This index is a function of the air pressure, air temperature, and water vapor partial pressure. At sea level in midlatitudes, a typical value of n is 1.000 35, and so it is conventional to work with the refractivity $N = (n - 1) \times 10^6$. The refractivity corresponding to $n = 1.000\ 35$ is then $N = 350$ N units. In dry air, the refractive index has the same value over almost the entire range of the electromagnetic spectrum. However, when water vapor is present, the refractive index of the moist air becomes frequency dependent, being greater for radio waves than for optical frequencies. A semiempirical formulation to calculate the atmospheric refractivity for radio waves was given by Bean and Dutton (1968):

$$N = \frac{77.6}{T}\left(p + 4810\frac{e}{T}\right), \tag{1}$$

in which T is the air temperature (K), p is the air pressure (hPa), and e is the water vapor pressure (hPa). A modified refractivity M can be defined to take account of the earth's curvature. It is given by

$$M = N + \frac{z}{R} \times 10^6, \tag{2}$$

where z is the height above sea level (m) and R is the mean radius of the earth (km). A ray emitted at a small angle to the ground will be bent toward (or away from) the local horizon if the modified refractivity decreases (or increases) with height. If sufficient bending toward the ground occurs, the ray may become trapped in a duct.

Turton et al. (1988) presented a classification of different atmospheric propagation conditions and radio ducting effects. Five main types of meteorological process may lead to duct formation: 1) evaporation over the sea; 2) anticyclonic subsidence; 3) subsidence at frontal surfaces; 4) nocturnal radiative cooling over

Corresponding author address: B. W. Atkinson, Dept. of Geography, Queen Mary and Westfield College, University of London, London E1 4NS, United Kingdom.
E-mail: b.w.atkinson@qmw.ac.uk

land; and 5) advection. Evaporation ducts are frequently observed over the oceans because of the large lapse of humidity normally present immediately above the sea surface. They exhibit geographical, seasonal, and diurnal variations, with greater depths at lower latitudes, during the summer months, and during the daytime (Babin et al. 1997). Ducts resulting from nocturnal radiative cooling are associated with temperature inversions. Dew deposition and fog development also affect the ducting conditions in the nocturnal ABL. Advection ducts may form when warm, dry continental air passes over a cooler sea, thus cooling and moistening the lowest layers. When the warm air from a dry landmass moves over the cooler sea water, a stable internal boundary layer (IBL) forms (Garratt 1990). As this IBL forms over water it is called a marine internal boundary layer (MIBL). The moisture accumulated in the stable surface layer is a major cause of a decrease in radar refractive index with height and the formation of a radar duct with a depth approximately equal to that of the MIBL. These are frequently surface ducts (Fig. 1). This effect may reinforce a preexisting evaporation duct and so increase its depth. Advection ducts can also be observed when warm moist air is advected over a cooler sea, resulting in the formation of sea fog with a duct near the top of the fog.

Despite observational programs [such as those reported by Babin and Rowland (1992); Babin (1995, 1996); Christophe et al. (1995); Craig and Hayton (1995); and Dockery and Goldhirsh (1995)] and the existence of numerical radar propagation models, forecasting the propagation environment remains a significant problem (Levy and Craig 1992). The most difficult aspect is the prediction of realistic refractivity fields, a view expressed by Christophe et al. (1995) who argued that obtaining meteorological profiles is currently a more important task than assessing them in radar models. The application of several mesoscale models has been investigated in this context. Burk and Thompson (1995, 1997) modeled the summertime refractive conditions in the Southern California Bight, using the Navy Operational Regional Atmospheric Prediction System. Despite the coarse horizontal spacing (20 km), a sea–land breeze that was generally in agreement with coastal station observations was simulated. Model simulation of the trapping layer (TL) showed significant diurnal variations in the marine boundary layer (MBL) along the central coastal portion of the Southern California Bight, but such variations diminished rapidly away from the coast. These results encouraged the use of an *M*-field predicted by a mesoscale model as input to radio propagation models for forecasting the propagation environment. As argued by Rogers (1995), the horizontal variation of refractivity is another imperative for accurate prediction of the coastal propagation environment (Barrios 1995; Cook et al. 1995). Lystad and Tjelta (1995) simulated the refractivity field over a coastal area of Norway at about 65°N. In comparison with radiosonde measurements, their model proved to be useful in predicting the spatial distributions and diurnal variations of refractivity, but it missed the fine vertical structures that are also of critical importance for radio propagation.

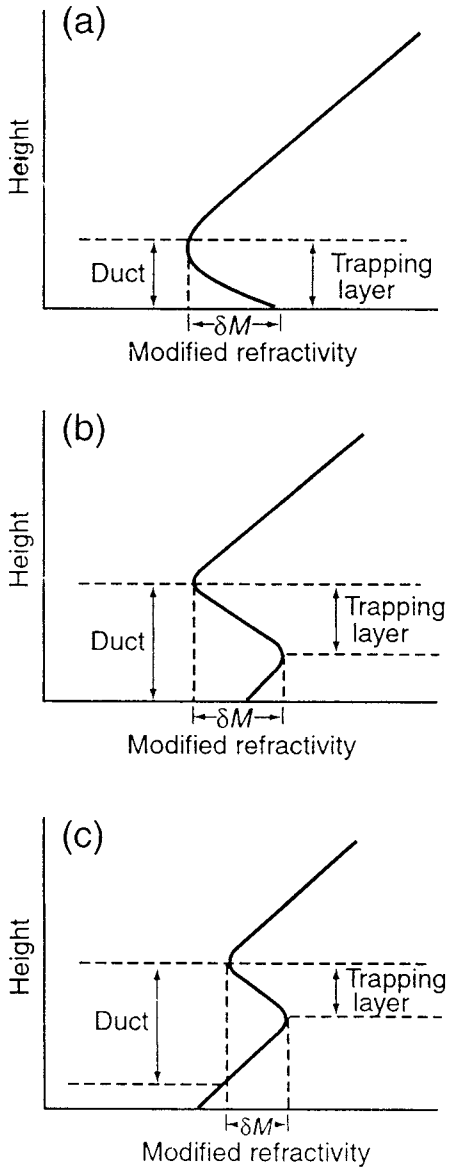

FIG. 1. Typical modified refractivity *M* profiles for (a) simple surface duct, (b) surface S-shaped duct, and (c) elevated duct. The depths of the ducts and the trapping layers are indicated (after Turton et al. 1988).

This paper aims to analyze the meteorological environment that could affect propagation conditions through the use of a nonhydrostatic, fine-resolution mesoscale model. It presents the results of simulations of the environment in the Persian Gulf on the occasions of research flights in that area. Observations of meteorological and radio-wave-propagation conditions over coastal waters were taken in the Persian Gulf by the

U.K. Meteorological Office C-130 Hercules aircraft during the Ship Antisubmarine Warfare Readiness/Effectiveness Measuring (SHAREM-115) exercise in April 1996. The primary aim of the SHAREM-115 research flights was to investigate the structure and variability of the stable IBL formed in northwesterly winds over the Persian Gulf. Results from this exercise were reported by Brooks et al. (1999) and by Brooks and Rogers (2000). These observations provide a detailed, high-quality dataset with which to compare the simulation results. The five research flights conducted during SHAREM-115 may be conveniently split into two groups according to the boundary layer conditions. The flights on 23 and 25 April were characterized by relatively low wind speeds (hereinafter known as ''low-wind'' cases), typically from 5 to 10 m s^{-1}, and an inversion at a height 100 m or less. The flights on 27, 28, and 29 April were characterized by higher wind speeds (hereinafter known as ''high-wind'' cases) of up to about 23 m s^{-1} and a deeper surface layer with an inversion at 200–300 m.

In this study, three sets of numerical experiments were conducted. Each set comprised low- and high-wind cases in northwesterly airflow from the land to the west of the Persian Gulf. In both cases the wind profiles were smoothed composites of a sounding at Kuwait International Airport (KIA) and the winds observed by the ship U.S.S. *Caron* and by the aircraft in SHAREM-115. These profiles were used in all the sets. The first set (set 1) used idealized but realistic profiles of temperature and humidity to assess the capability of the model to capture the essentials of the boundary layer and duct conditions in the Gulf area. The second (set 2) used particular radiosonde ascents from KIA to initialize the model, and the third (set 3) used combinations of particular radiosonde ascents and the SHAREM-115 data for initialization.

Section 2 summarizes the model and the configuration used in the simulations. Sections 3 and 4 present the results and discussion, and section 5 gives the conclusions.

2. The mesoscale model

The model used in this study (Ballard et al. 1991; Golding 1987, 1990) is nonhydrostatic, three-dimensional, and semi-implicit (Tapp and White 1976), with higher-order closure and a terrain-following coordinate scheme (Carpenter 1979). It has been thoroughly tested and successfully used in mesoscale studies by Atkinson (1995), Atkinson and Shahub (1994), Dare and Atkinson (1999), and Li and Atkinson (1999). The lower boundary conditions used in the model were based on Monin–Obukhov similarity theory. Lateral boundary conditions for the velocity components were different for the normal and tangential components. The normal components were specified. The normal gradient of the horizontal tangential velocity was set to zero at the lateral boundaries. Zero-gradient lateral boundary conditions were also applied to the potential temperature, surface temperature, Exner pressure, and specific humidity. The top boundary was placed 10 km above the surface so as not to interfere with the thermally induced coastal circulations. Test runs confirmed that the simulated circulations over land surfaces were all confined below 4 or 5 km by the stable stratification above the mixing layer, which was about 1.5 km deep. Horizontal velocity and potential temperature at the top boundary were held fixed at their initial values.

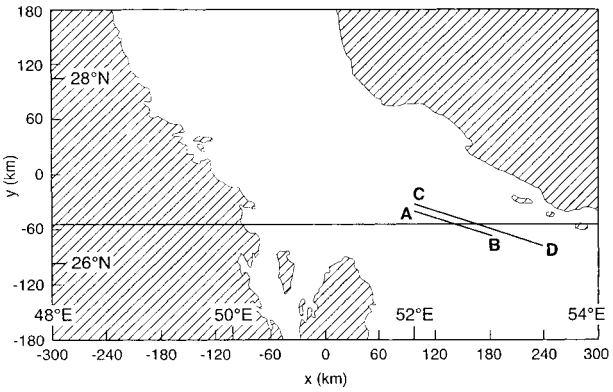

FIG. 2. Domain used in the simulations. The area is part of the Persian Gulf. Land is shaded. The line at $y = -54$ km is the location of cross sections of simulated results shown in section 3. Line AB is the location of cross sections in Figs. 10 and 11. Line CD is the location of cross sections in Figs. 13 and 14.

The model domain was chosen to cover the central part of the Persian Gulf (Fig. 2), where aircraft observations were made in 1996 (Brooks et al. 1999; Brooks and Rogers 2000). The horizontal domain was centered at 27°N, 51°E and covered an area of 600 × 360 km^2 with a grid length of 6 km. Sensitivity studies have shown that grid lengths as coarse as 15 km can be used for qualitative studies of the propagation environment but the strong gradients associated with the MIBL are more accurately captured at fine resolution. Thirty-three vertical levels were chosen, with spacing that increased with height to ensure good resolution at low altitudes (Table 1). This spacing may be compared with the 14 levels used in the study of Lystad and Tjelta (1995), a limitation that those authors considered to have hindered the ability of their model to capture important details in the vertical structure of the propagation environment.

The land surface within the domain was approximated as uniform desert sand with an albedo of 0.36 and a surface roughness length of 1 mm. Its temperature was determined from a surface heat budget. Surface resistance to evaporation was initialized at 1000 m^{-1} s, which represents a dry sand surface. The sea surface temperature was held fixed, and the roughness length over the sea was determined through Charnock's relation (Wu 1982).

TABLE 1. Model levels and initial conditions of potential temperature θ, temperature T, and mixing ratio MR in set 1.

Level	z (m)	θ (°C)	T (°C)	MR (g kg^{-1})
1	10.0	22.75	22.65	13.62
2	20.0	23.00	22.80	13.31
3	40.0	23.50	23.10	12.62
4	60.0	24.00	23.40	12.18
5	80.0	24.50	23.70	11.57
6	100.0	25.00	24.00	10.93
7	130.0	25.75	24.44	9.90
8	160.0	26.50	24.89	8.81
9	190.0	27.25	25.33	7.63
10	220.0	28.00	25.77	6.37
11	260.0	29.00	26.36	4.56
12	300.0	30.00	26.94	2.72
13	350.0	30.30	26.74	2.67
14	400.0	30.60	26.53	2.53
15	450.0	30.90	26.32	2.50
16	500.0	31.20	26.11	2.47
17	600.0	31.80	25.68	2.41
18	800.0	33.00	24.84	2.27
19	1000.0	34.20	24.00	2.18
20	1300.0	36.00	22.72	2.03
21	1600.0	37.80	21.45	1.88
22	1900.0	39.60	20.17	1.74
23	2200.0	41.40	18.88	1.60
24	2600.0	43.80	17.16	1.44
25	3000.0	46.20	15.44	1.29
26	3500.0	49.20	13.27	1.12
27	4000.0	52.20	11.10	0.96
28	5000.0	58.20	6.73	0.67
29	6000.0	64.20	2.34	0.48
30	7000.0	70.20	−2.07	0.33
31	8000.0	76.20	−6.49	0.20
32	9000.0	82.20	−10.92	0.12
33	10 000.0	88.20	−15.35	0.05

3. Results

a. Set 1

For this set of experiments, soundings of temperature and humidity from KIA, the ship U.S.S. *Caron*, and the aircraft in SHAREM-115 allowed the specification of a profile of the spring atmosphere over the Gulf (Table 1). By both design and necessity, this profile did not describe conditions at one place at a particular time, but was representative of atmospheric conditions over the Gulf at the time of the SHAREM-115 flights. The profile was used to describe horizontally homogeneous conditions throughout the model domain and was used for both high- and low-wind cases. Runs were initialized at 0700 local time (LT), a time for which SHAREM-115 data were available, and also a time of day when land–sea thermal contrasts are usually small.

1) LOW-WIND CASE

The juxtaposition of hot, dry land with water in the Gulf region favors strong contrasts between the land and marine boundary layers. In such situations air flowing from the land to the sea is substantially cooled, stabilized, and moistened as an MIBL forms over the water surface (Rogers et al. 1995). The different characteristics of the boundary layer over land and sea were well captured by the model. Over the land area, a mixed boundary layer about 1-km deep with potential temperatures of about 34°C (Fig. 3a) was associated with vertically uniform mixing ratios of about 6 g kg^{-1} (Fig. 3b) and a linearly increasing refractivity (Fig. 3c). In contrast, the lowest 300 m over the sea showed a temperature inversion of about 8°C (Fig. 3a), moistening of the air near the surface with mixing ratios reaching about 16 g kg^{-1} (Fig. 3b), and a lapse of refractivity (Fig. 3c). Garratt and Ryan (1989) noted that such stable layers may be only a few hundreds of meters deep after fetches of 500 km or more.

Figure 4 shows the development of the MBL in the profiles of potential temperature, mixing ratio, and refractivity at the point $x = 210$ km, $y = -78$ km far out to sea. By midafternoon, the isentropic layer was about 100 m deep, and the capping inversion had strengthened to about 0.1°C m^{-1} between 100 and 140 m. Evolution of the water vapor profiles at the same sea point (Fig. 4b) showed that a near-constant mixing ratio was maintained in the marine surface layer. Above about 150 m the simulations showed dry air, possibly caused by subsidence associated with the seaward part of a sea-breeze circulation (SBC). The simulated profiles of refractivity (Fig. 4c) showed a simple surface duct (Fig. 1a) about 100–160-m deep, similar to the surface duct observed on 23 April 1996 in the Persian Gulf (Brooks et al. 1999).

2) HIGH-WIND CASE

In the high-wind simulation, the profile of potential temperature (Fig. 5a) revealed the development by midday of an MIBL about 200 m deep overlain by a sharp inversion. The stable layer was about twice as deep as the one formed in the low-wind case. The simulated moist near-surface layer (Fig. 5b) was also about 200 m deep and was overlain by air with humidity of about 3 g kg^{-1}. In the refractivity profile (Fig. 5c) an S-shaped duct (Fig. 1b) was evident, in which the trapping and duct layers were about 100 and 300 m in depth, respectively. Near the shoreline, a simple surface duct occurred in the evolving MIBL, and the S-shaped duct became apparent beyond a fetch of about 100 km. Some preliminary investigations of the model refractivity profiles using a radar propagation model (Craig 1988; Levy 1995) revealed that the existence of a transition between the two kinds of duct had significant effects on propagation. For example, the trapping of radar signals sent from land to sea through the growing duct becomes notably more efficient once the character of the duct changes to an S shape.

Comparison of the results from set 1 with the data from SHAREM-115 was encouraging. Despite the horizontally homogeneous initial conditions the model had

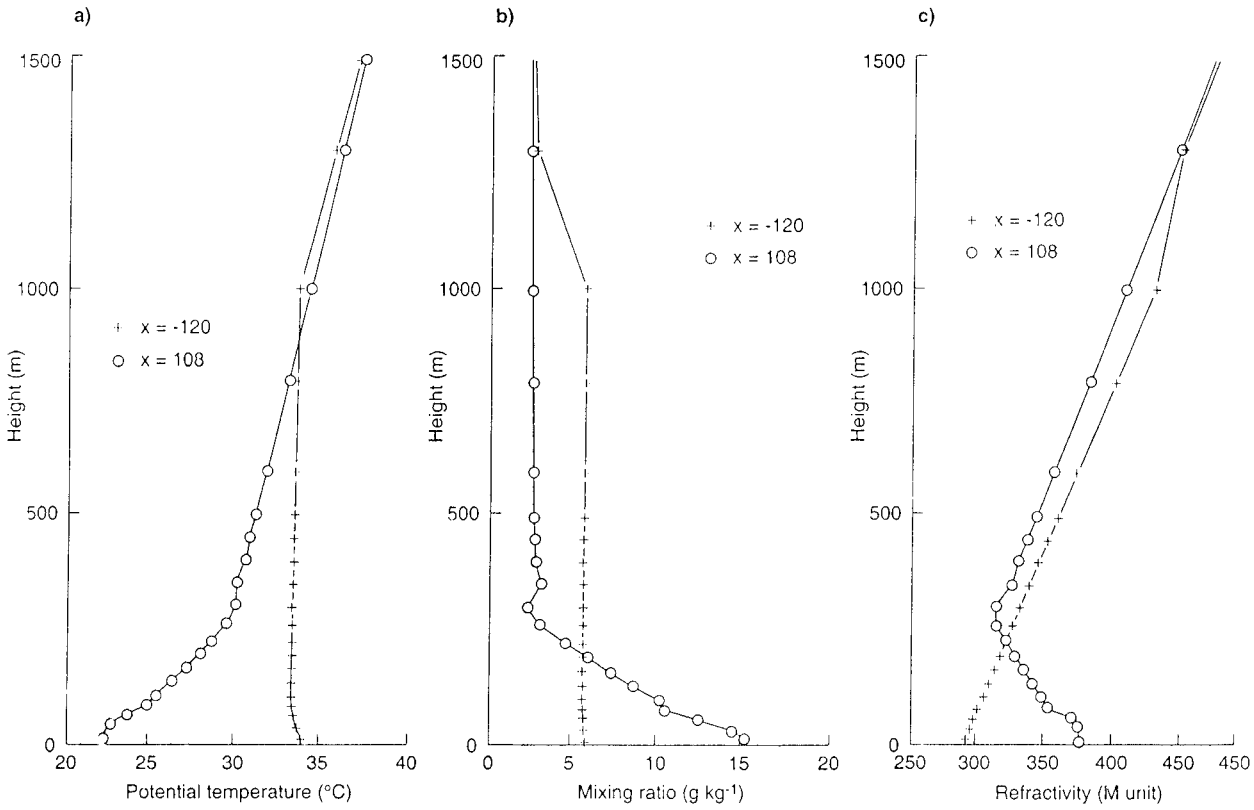

FIG. 3. Profiles for 1500 LT along $y = -54$ km at points $x = -120$ km (land) and $x = 108$ km (sea): (a) potential temperature (°C), (b) humidity (g kg^{-1}), and (c) refractivity (M unit).

clearly distinguished the boundary layers over land and water. Over the Gulf, the boundary layer was significantly cooler and moister than the equivalent over land, and the shape of the potential temperature profile indicated that the cooling was caused by turbulent transfer (André and Mahrt 1982). In addition, the model distinguished the different depths of the MIBL and associated ducts in the low- and high-wind cases, as found in the

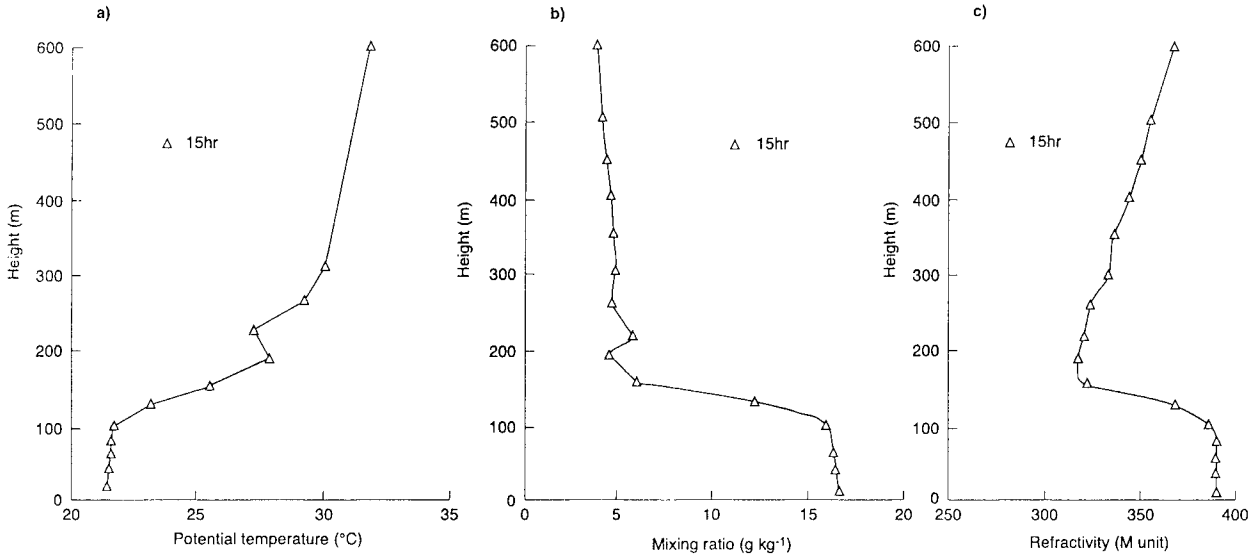

FIG. 4. Profiles for 1500 LT of simulated values in low-wind case at $x = 210$ km, $y = -78$ km: (a) potential temperature (°C), (b) humidity (g kg^{-1}), and (c) refractivity (M unit).

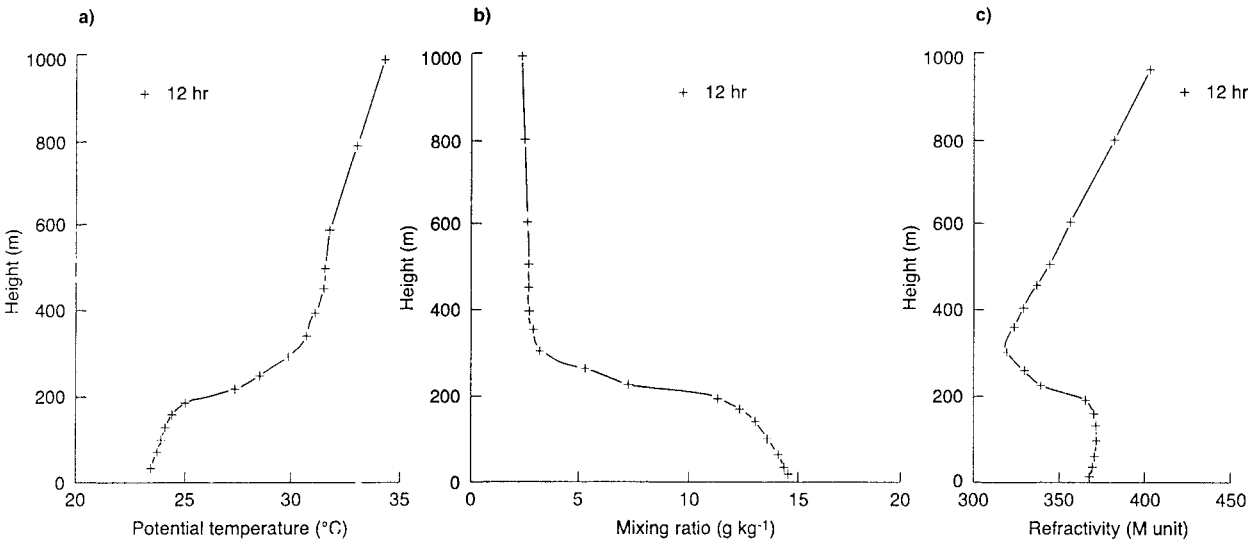

FIG. 5. Profiles for 1200 LT of simulated values in high-wind case at $x = 210$ km, $y = -78$ km: (a) potential temperature (°C), (b) humidity (g kg^{-1}), and (c) refractivity (M unit).

TABLE 2. Model levels and initial conditions of potential temperature θ, temperature T, and mixing ratio MR in the low-wind case of set 2.

Level	z (m)	θ (°C)	T (°C)	MR (g kg^{-1})
1	10.0	25.03	24.93	7.21
2	20.0	25.06	24.86	7.16
3	40.0	25.11	24.70	7.10
4	60.0	25.16	24.55	6.92
5	80.0	25.21	24.40	6.82
6	100.0	25.26	24.25	6.70
7	130.0	25.33	24.02	6.53
8	160.0	25.41	23.80	6.38
9	190.0	25.51	23.60	6.25
10	220.0	25.81	23.60	6.25
11	260.0	26.22	23.60	6.26
12	300.0	26.62	23.60	6.27
13	350.0	27.13	23.60	6.29
14	400.0	27.64	23.60	6.30
15	450.0	28.14	23.60	6.31
16	500.0	28.65	23.60	6.32
17	600.0	29.67	23.60	6.34
18	800.0	31.73	23.60	6.40
19	1000.0	33.63	23.44	5.79
20	1300.0	35.19	21.95	2.69
21	1600.0	36.11	19.84	2.89
22	1900.0	37.01	17.73	3.04
23	2200.0	37.79	15.52	3.14
24	2600.0	38.15	11.98	3.29
25	3000.0	38.46	8.43	3.29
26	3500.0	39.19	4.37	1.65
27	4000.0	39.43	−0.07	2.33
28	5000.0	39.69	−8.92	3.02
29	6000.0	43.63	−14.48	1.07
30	7000.0	46.58	−20.74	0.21
31	8000.0	48.18	−27.91	0.11
32	9000.0	49.66	−34.96	0.29
33	10 000.0	51.73	−41.39	0.18

SHAREM-115 program. These results encouraged further testing with other initial conditions.

b. Set 2

In these experiments, the initial conditions differed from those of set 1 in two ways. First, the runs were initialized with temperatures and humidities from particular radiosonde ascents at KIA. Second, the surface temperatures over sea and land were determined from the sea surface temperatures (SSTs) reported by Brooks et al. (1999) and the synoptic observations at KIA, respectively. The set-2 initial conditions describe the upstream, overland atmosphere, in marked contrast to those of set 1, which represented the downstream, marine atmosphere. Because the set-2 configuration contained no information on the MBL, any MIBL seen in the results from this set could have evolved only through the action of modeled processes.

1) LOW-WIND CASE

The low-wind run was initialized with the 0000 UTC (0300 LT) ascent at KIA on 23 April 1996 (Table 2). Figure 6 shows profiles of simulated potential temperature, mixing ratio, and refractivity, together with observed values at the point $x = 210$, $y = -78$ km in the early afternoon. A mixed layer about 300-m deep developed with a potential temperature of about 25.5°C, roughly equal to the SST (Fig. 6a). This mixed boundary layer was capped by an inversion with a potential temperature difference across it of only 2°C. Potential temperatures in the lowest 70 m compared well with observed values, but above that height the simulated values were much lower than those observed. Thus the modeled thermal boundary layer was too deep and too cold.

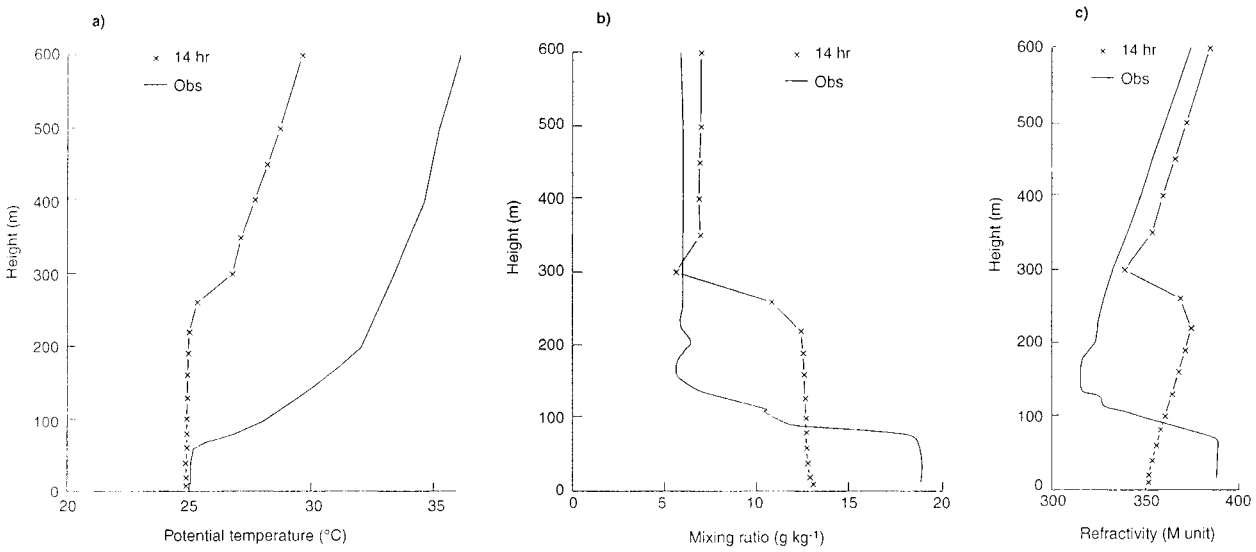

FIG. 6. Profiles for 1400 LT of simulated and observed values at $x = 210$ km, $y = -78$ km in the low-wind case of set 2. The observations were for 1415–1425 LT 23 Apr 1996, taken in SHAREM-115 (I. M. Brooks 1999, personal communication): (a) potential temperature (°C), (b) humidity (g kg^{-1}), and (c) refractivity (M unit).

TABLE 3. Model levels and initial conditions of potential temperature θ, temperature T, and mixing ratio MR in the high-wind case of set 2.

Level	z (m)	θ (°C)	T (°C)	MR (g kg^{-1})
1	10.0	20.58	20.48	5.70
2	20.0	21.22	21.02	5.45
3	40.0	22.50	22.10	4.87
4	60.0	23.47	22.87	4.45
5	80.0	23.84	23.04	4.47
6	100.0	24.18	23.17	4.33
7	130.0	24.68	23.38	4.20
8	160.0	25.19	23.58	4.03
9	190.0	25.69	23.78	3.85
10	220.0	25.82	23.61	3.81
11	260.0	25.93	23.32	3.77
12	300.0	26.05	23.03	3.74
13	350.0	26.19	22.67	3.69
14	400.0	26.33	22.31	3.65
15	450.0	26.47	21.95	3.58
16	500.0	26.61	21.59	3.56
17	600.0	26.89	20.87	3.47
18	800.0	27.40	19.38	3.20
19	1000.0	27.74	17.75	2.78
20	1300.0	28.69	15.73	2.83
21	1600.0	30.12	14.17	3.52
22	1900.0	31.18	12.26	3.65
23	2200.0	31.94	10.10	4.82
24	2600.0	33.37	7.60	5.46
25	3000.0	36.70	6.85	1.62
26	3500.0	38.22	3.50	1.54
27	4000.0	39.82	0.27	1.31
28	5000.0	43.23	−5.93	0.83
29	6000.0	45.93	−12.60	0.43
30	7000.0	45.96	−21.23	0.26
31	8000.0	45.79	−29.73	0.11
32	9000.0	48.42	−35.87	0.03
33	10 000.0	51.13	−41.82	0.02

Associated with the mixed thermal layer, a moist, marine boundary layer existed below about 300 m (Fig. 6b). It was about 3 times deeper than that observed, and the near-surface magnitudes were underestimated by about 6 g kg^{-1}. In the initial conditions of set 2, the humidity at low altitudes is significantly less than in set 1, but the humidity over the sea increases through the action of evaporation in the model. Comparison of the areas beneath the curves on Fig. 6b suggests that the model captured the rate of surface evaporation well but that in the model the water vapor was mixed through a deeper layer than in nature. A refractivity profile exhibiting surface ducting was produced below 300 m, a height slightly more than 2 times that observed. This occurred because the refractivity profile follows that of the humidity to a large degree, leading to underprediction of M below about 100 m and overprediction above that height.

2) HIGH-WIND CASE

The high-wind run was initialized from the 0000 UTC (0300 LT) ascent at KIA on 28 April 1996 (Table 3). Simulated and observed profiles are shown in Fig. 7 for the point $x = 186$, $y = -54$ km in the early afternoon. The potential temperature in the mixed layer was about 24°C, in accordance with the SST. The boundary layer generated in the run was about 600-m deep, capped by a weak inversion. Observations reveal (Fig. 7a) that the simulated temperatures were correct in the lowest 200 m of the boundary layer but that the height and strength of the capping inversion were, respectively, too large and too small. The simulated magnitudes of humidity below about 200 m were in good agreement with observations (Fig. 7b), but the sharp lapse observed be-

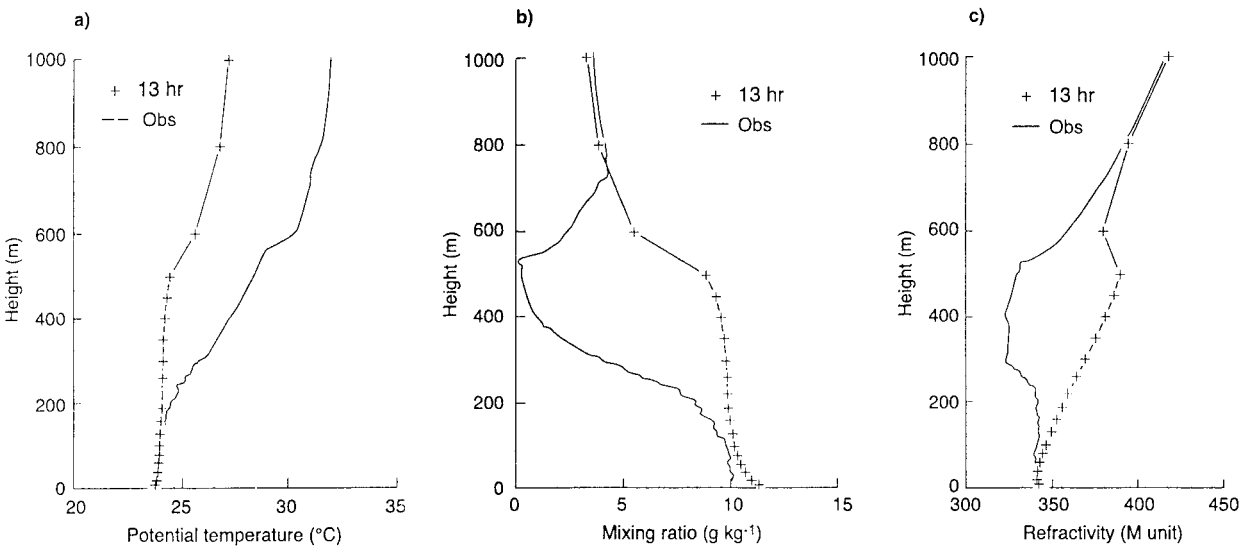

FIG. 7. Profiles for 1300 LT of simulated and observed values at $x = 186$ km, $y = -54$ km in the high-wind case of set 2. The observations were for 1301–1307 LT 28 Apr 1996, taken in SHAREM-115 (I. M. Brooks 1999, personal communication): (a) potential temperature (°C), (b) humidity (g kg^{-1}), and (c) refractivity (M unit).

tween 200 and 500 m was not captured in the simulations. Because the refractivity is strongly dependent on the humidity, its profile also did not display the strong lapse above 200 m, but the magnitudes below that height were captured in the simulation. A TL was found between 500 and 600 m, giving an elevated duct (Fig. 1c) between 400 and 600 m, in contrast to the observed surface duct below about 270 m.

c. Set 3

In set 2, the land–sea contrast was recognized by the use of different values for the SST and the land temperature. The thermal and humidity conditions in the lowest few hundred meters of the atmosphere were interpolated from those surface values and data recorded at low levels in a KIA sounding. In set 3, the initial states of the marine boundary layers in the low- and high-wind cases were specified from the SHAREM-115 observations. The initial state of the land boundary layer was derived from the KIA sounding and KIA synoptic observations. Runs were initialized at 0700 LT, a time for which SHAREM-115 data were available, and predicted conditions for the following afternoon, when other SHAREM-115 observations were available for comparison. Only one set of 0700 LT data, taken on a high-wind day, was available from SHAREM-115. In the absence of other appropriate data, these data were used in both the low- and high-wind runs.

1) LOW-WIND CASE

The initial conditions for temperature and humidity were largely derived from the 0000 UTC (0300 LT) sounding at KIA on 23 April 1996. This sounding was taken 4 h before the start of the run, but comparison of the 0000 and 1200 UTC soundings revealed very small differences in temperature and humidity above a height of 1 km. Below that height, the land profile was derived from the ascent and the surface conditions observed at 0700 LT at KIA. Over the sea, the SHAREM-115 observations for around 0700 LT on 28 April 1996 were used to describe conditions below 1 km. The data are shown in Table 4.

Figure 8a compares predicted afternoon profiles of potential temperature with observations from SHAREM-115 at 1415–1425 LT on 23 April 1996 at the point $x = 210$, $y = -78$ km. A simulated mixed boundary layer with a depth of 100 to 130 m was capped by an inversion, which was most marked between 130 and 200 m. Observations showed a mixed layer of about 70 m in depth, overlain by a strong inversion of about 8°C between 130 and 200 m. The predicted humidity profiles (Fig. 8b) showed a moist MIBL below about 130 m with the magnitudes close to the surface being underpredicted. The refractivity profile (Fig. 8c) followed that of the humidity closely. Although the run underpredicted M magnitudes throughout the MIBL and consequently also the strength of the capping lapse, the surface duct is clearly captured. Its depth was overpredicted by a maximum of about 60 m. In view of the fact that the low-level initial conditions for this case were necessarily taken from data on a high-wind day, the above results are encouraging.

2) HIGH-WIND CASE

The initial conditions for the high-wind case were largely derived from the 0000 UTC (0300 LT) sounding at KIA on 28 April 1996. As in the low-wind case,

TABLE 4. Model levels and initial conditions of potential temperature θ, temperature T, and mixing ratio MR in the low-wind case of set 3.

		Sea			Land		
Level	z (m)	θ (°C)	T (°C)	MR (g kg^{-1})	θ (°C)	T (°C)	MR (g kg^{-1})
1	10.0	25.48	25.38	10.50	27.40	27.29	7.01
2	20.0	25.31	25.11	10.23	27.29	27.08	6.93
3	40.0	25.17	24.77	10.16	27.07	26.66	6.88
4	60.0	25.23	24.62	10.16	26.85	26.24	6.79
5	80.0	25.28	24.48	10.15	26.63	25.81	6.70
6	100.0	25.34	24.33	10.17	26.41	25.39	6.62
7	130.0	25.64	24.33	9.89	26.08	24.76	6.42
8	160.0	25.94	24.33	8.31	25.75	24.13	6.35
9	190.0	26.24	24.32	7.39	25.52	23.60	6.25
10	220.0	26.84	24.62	6.07	25.82	23.60	6.25
11	260.0	27.84	25.21	4.04	26.23	23.60	6.26
12	300.0	28.84	25.80	2.02	26.63	23.60	6.27
13	350.0	29.84	26.28	1.03	27.14	23.60	6.29
14	400.0	30.84	26.76	0.10	27.65	23.60	6.30
15	450.0	31.49	26.89	0.10	28.15	23.60	6.31
16	500.0	32.14	27.03	0.10	28.66	23.60	6.32
17	600.0	33.34	27.19	0.10	29.69	23.60	6.34
18	800.0	34.14	25.95	3.02	31.74	23.60	6.40
19	1000.0	34.14	23.93	3.02	33.63	23.43	5.79
20	1300.0	35.19	21.95	2.69	35.19	21.95	2.69
21	1600.0	36.11	19.84	2.89	36.11	19.84	2.89
22	1900.0	37.01	17.73	3.04	37.01	17.73	3.04
23	2200.0	37.79	15.52	3.14	37.79	15.52	3.14
24	2600.0	38.15	11.98	3.29	38.15	11.98	3.29
25	3000.0	38.46	8.43	3.29	38.46	8.43	3.29
26	3500.0	39.19	4.37	1.65	39.19	4.37	1.65
27	4000.0	39.43	−0.07	2.33	39.43	−0.07	2.33
28	5000.0	39.69	−8.92	3.02	39.69	−8.92	3.02
29	6000.0	43.63	−14.48	1.07	43.64	−14.48	1.07
30	7000.0	46.58	−20.74	0.21	46.58	−20.74	0.21
31	8000.0	48.18	−27.91	0.11	48.18	−27.91	0.11
32	9000.0	49.66	−34.96	0.29	49.66	−34.96	0.29
33	10 000.0	51.73	−41.39	0.18	51.73	−41.39	0.18

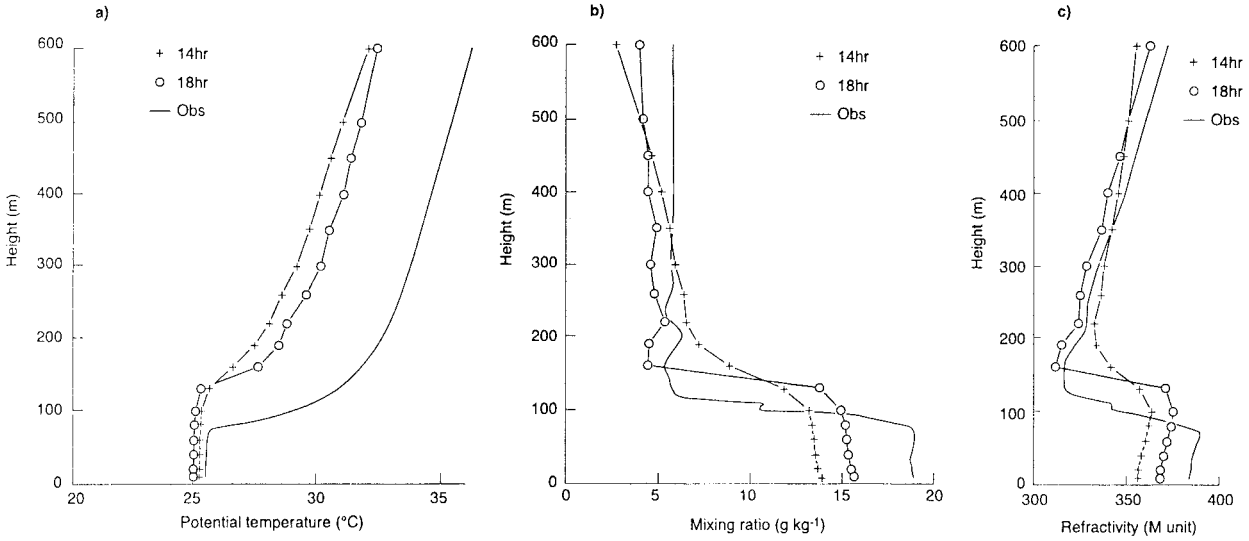

FIG. 8. Profiles for 1400 and 1800 LT of simulated and observed values at $x = 210$ km, $y = -78$ km in the low-wind case of set 3. The observations were for 1415–1425 LT 23 Apr 1996, taken in SHAREM-115 (I. M. Brooks 1999, personal communication): (a) potential temperature (°C), (b) humidity (g kg^{-1}), and (c) refractivity (M unit).

TABLE 5. Model levels and initial conditions of potential temperature θ, temperature T, and mixing ratio MR in the high-wind case of set 3.

		Sea			Land		
Level	z (m)	θ (°C)	T (°C)	MR (g kg^{-1})	θ (°C)	T (°C)	MR (g kg^{-1})
1	10.0	24.01	23.91	10.49	25.52	25.41	4.47
2	20.0	24.58	24.38	10.33	25.53	25.32	4.44
3	40.0	25.17	24.77	10.16	25.56	25.15	4.36
4	60.0	25.23	24.62	10.16	25.58	24.97	4.32
5	80.0	25.28	24.48	10.15	25.61	24.79	4.23
6	100.0	25.34	24.33	10.17	25.63	24.61	4.15
7	130.0	25.64	24.33	9.34	25.67	24.35	4.03
8	160.0	25.94	24.33	7.80	25.70	24.08	3.92
9	190.0	26.24	24.32	7.80	25.74	23.82	3.83
10	220.0	26.84	24.62	6.07	25.82	23.60	3.81
11	260.0	27.84	25.21	4.02	25.94	23.31	3.77
12	300.0	28.84	25.80	2.02	26.05	23.02	3.73
13	350.0	29.84	26.28	1.06	26.19	22.66	3.69
14	400.0	30.84	26.76	0.10	26.33	22.30	3.65
15	450.0	31.49	26.89	0.10	26.47	21.94	3.60
16	500.0	32.14	27.03	0.10	26.61	21.58	3.56
17	600.0	33.34	27.19	0.10	26.89	20.86	3.47
18	800.0	34.14	25.95	3.02	27.40	19.38	3.23
19	1000.0	34.14	23.93	3.02	27.75	17.74	2.78
20	1300.0	34.58	21.36	4.09	28.70	15.72	2.83
21	1600.0	34.99	18.78	4.74	30.13	14.16	3.52
22	1900.0	35.39	16.21	4.72	30.13	14.16	3.52
23	2200.0	35.76	13.63	6.50	31.18	12.26	3.65
24	2600.0	36.21	10.20	6.50	33.38	7.60	5.47
25	3000.0	36.70	6.85	1.63	36.70	6.85	1.63
26	3500.0	38.22	3.50	1.54	38.22	3.50	1.54
27	4000.0	39.82	0.27	1.29	39.83	0.27	1.29
28	5000.0	43.23	−5.93	0.83	43.23	−5.93	0.83
29	6000.0	45.93	−12.60	0.43	45.93	−12.60	0.43
30	7000.0	45.96	−21.23	0.26	45.96	−21.23	0.26
31	8000.0	45.79	−29.73	0.11	45.79	−29.73	0.11
32	9000.0	48.42	−35.87	0.03	48.43	−35.87	0.03
33	10 000.0	51.13	−41.82	0.02	51.13	−41.82	0.02

comparison of the 0000 and 1200 UTC soundings revealed very small changes over time in the temperature and humidity above 1 km. Below that height, the land profile was derived from the ascent and from the KIA surface observations and the sea profile was derived from SHAREM-115 data (Table 5).

Figure 9a shows the profiles of simulated and observed potential temperature in the lowest kilometer of the atmosphere. Up to 400 m, the prediction was good, having captured both the cool near-surface layer over the Gulf water and the lower part of the inversion that capped that layer. Temperatures in the higher levels of the inversion were underpredicted. The general shape of the humidity profile (Fig. 9b) is reasonable up to 300 m, but the model overpredicted the mixing ratio by 2–3 g kg^{-1}, and between 250 and 550 m, where the air was very dry, the overprediction increased to 4 g kg^{-1}. An MIBL was produced in the simulation, but its predicted top was not as sharply defined as in the observations. Predicted magnitudes of the refractivity above 700 m were in good agreement with observations. Below that height, the magnitudes were too large but the profile shape matched that of the observations well. The discrepancy between predictions and observations in this layer was largely caused by the profile of humidity. Despite the discrepancy, a surface duct was just discernible, and its depth was correctly simulated as 300 m.

d. Horizontal variation

Observations (Brooks et al. 1999) and model results have shown that horizontal variation in the MIBL may have a significant effect on the structure of the propagation environment. Previous studies of littoral refractivity environments using mesoscale models (Lystad and Tjelta 1995; Burk and Thompson 1995, 1997) have had access to verification data from only a few isolated locations within the model domain. The SHAREM-115 observations, however, are sufficiently detailed that vertical cross sections can be constructed through horizontal lengths of up to about 100 km (I. M. Brooks 1999, personal communication). Such cross sections are compared with the simulation results for both the low- and high-wind cases of set 3. The sections presented are of two lengths. The shorter ones, along the lines AB and CD shown in Fig. 2, enable comparison with the SHAREM-115 data. The longer sections allow identification

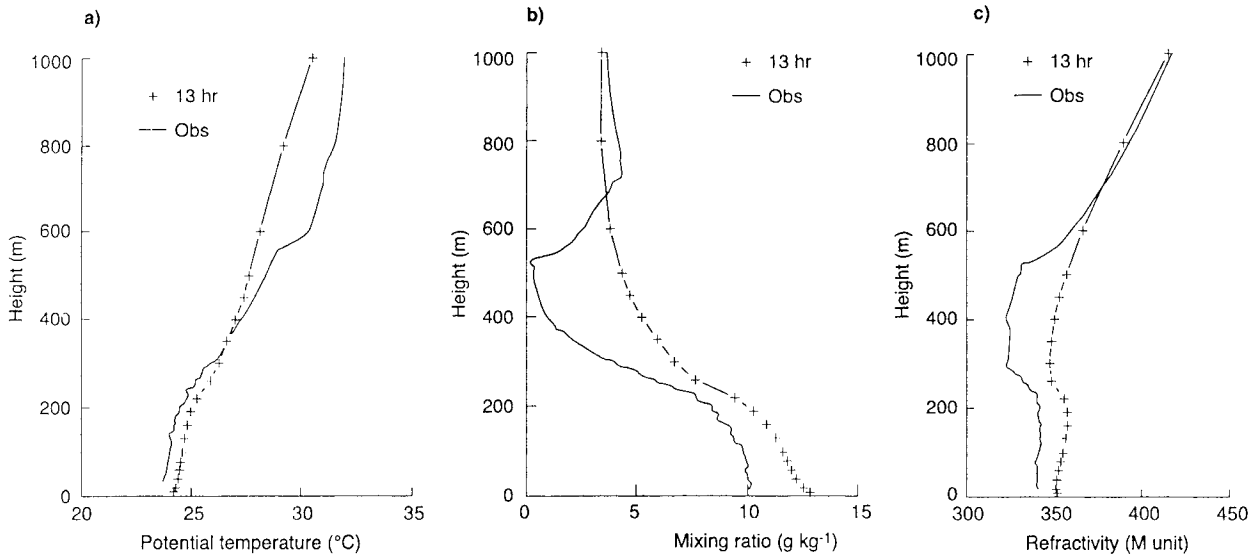

FIG. 9. Profiles for 1300 LT of simulated and observed values at $x = 186$ km, $y = -54$ km in the high-wind case of set 3. The observations were for 1301–1307 LT 28 Apr 1996, taken in SHAREM-115 (I. M. Brooks 1999, personal communication): (a) potential temperature (°C), (b) humidity (g kg^{-1}), and (c) refractivity (M unit).

of coastal effects and the larger-scale structure of the MIBL.

1) LOW-WIND CASE

Figures 10 and 11 show cross sections of the simulated and observed potential temperature and refractivity along the line AB in Fig. 2. The observed values in the figures (and those in Figs. 13 and 14) were kindly provided by I. M. Brooks (1999, personal communication). Appropriate cross sections were unavailable for 23 April 1996 so those for 25 April, also a low-wind day, were used instead. This, together with the use of high-wind SHAREM-115 data in the initial conditions, meant that some discrepancies between simulation and observations were to be expected. The distributions of potential temperature (Fig. 10) confirm that the simulated MIBL was deeper than that observed. As the run progressed, the depth of the layer decreased, suggesting that the anomaly introduced by the initial conditions was being rectified by the model processes. The anomaly may also have contributed to the lack of downwind slope in the inversion. In contrast, the intensity of the simulated temperature inversion capping the boundary layer is in good agreement with the observations. The section of simulated refractivity (Fig. 11a) shows the high values seen in the observations (Fig. 11b) for distances up to 40 km from A. Simulated low values beyond 50 km (Fig. 11a) lay at about 250 m, whereas in reality they lay between 100 and 200 m. For both variables, the observations revealed entrainment and wavelike features in the layer. Neither of these characteristics was captured by the simulation, probably because of three factors. First, the initial conditions over the Gulf were horizontally homogeneous. Second, entrainment usually occurs at scales smaller than the resolution used in these simulations. Third, the observed ''wavelengths'' were about 15 km but may have resulted from the aircraft sounding passing through shorter waves at small angles to the wave axes. Such shorter waves, possibly with wavelengths of a few kilometers, would also be missed by the simulation.

The longer cross section of the low-wind case showed distinct features in the distribution of potential temperature (Fig. 12a). First, over land the surface air temperatures were about 34°C and the lapse rate was dry adiabatic. Second, a marked horizontal gradient of temperature of about 6°C over 30 km occurred across the coastline. It was most distinct below about 200 m, and in that layer the isentropes were essentially vertical. Such characteristics accord with the well-known structure of sea breezes (Arritt 1993; Atkinson 1981; Bechtold et al. 1991; Finkele et al. 1995). The SHAREM-115 observations were made well away from the coastline so that nothing of the signature of the sea-breeze circulation was captured. However, the sea-breeze circulation is such a well-known phenomenon and the conditions in the Gulf are so favorable for its occurrence (Atkinson 1981) that it is highly likely that the simulations captured a real feature. A ''sea-breeze front'' (SBF), compatible with the model resolution, is identifiable in the vertical cross section of winds (Fig. 12d). The sea-breeze air was also evident in the section of humidity (Fig. 12b). The gradient of humidity at the SBF marked the landward edge of the sea air, complementing the stronger vertical gradient that capped the MIBL. The cross sections of simulated refractivity (Fig. 12c) reflected the striking vertical gradients seen in the

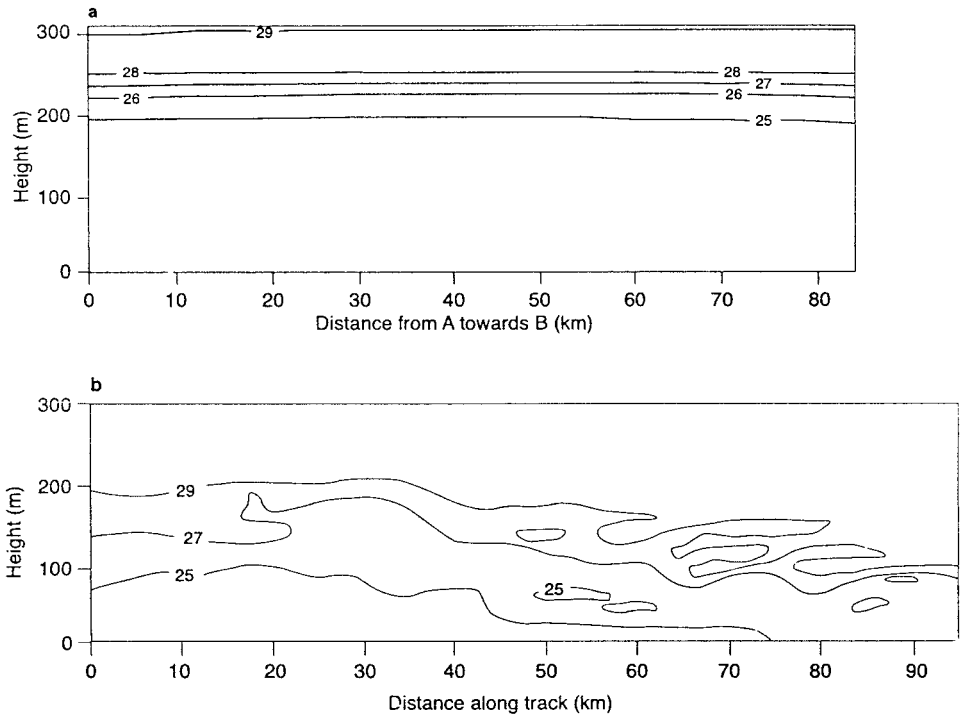

FIG. 10. Cross sections of potential temperature (°C) along line AB in Fig. 2 in the low-wind case of set 3: (a) simulated values at 1400 LT and (b) observations taken in SHAREM-115 on 25 Apr 1996.

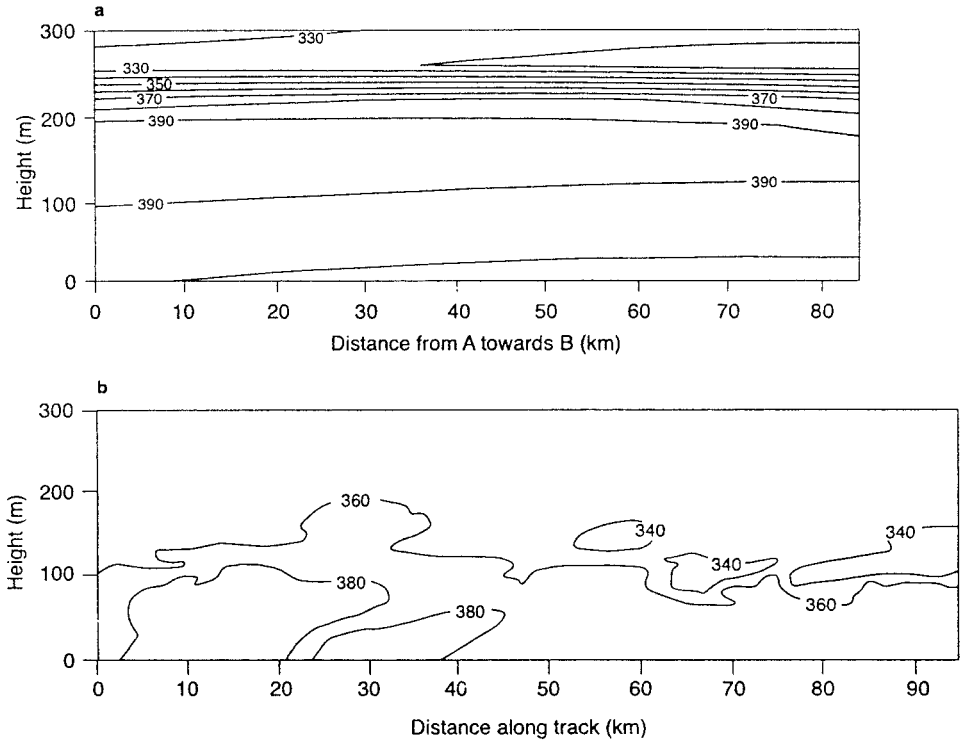

FIG. 11. Cross sections of refractivity (*M* unit) along line AB in Fig. 2 in the low-wind case of set 3: (a) simulated values at 1400 LT and (b) observations taken in SHAREM-115 on 25 Apr 1996.

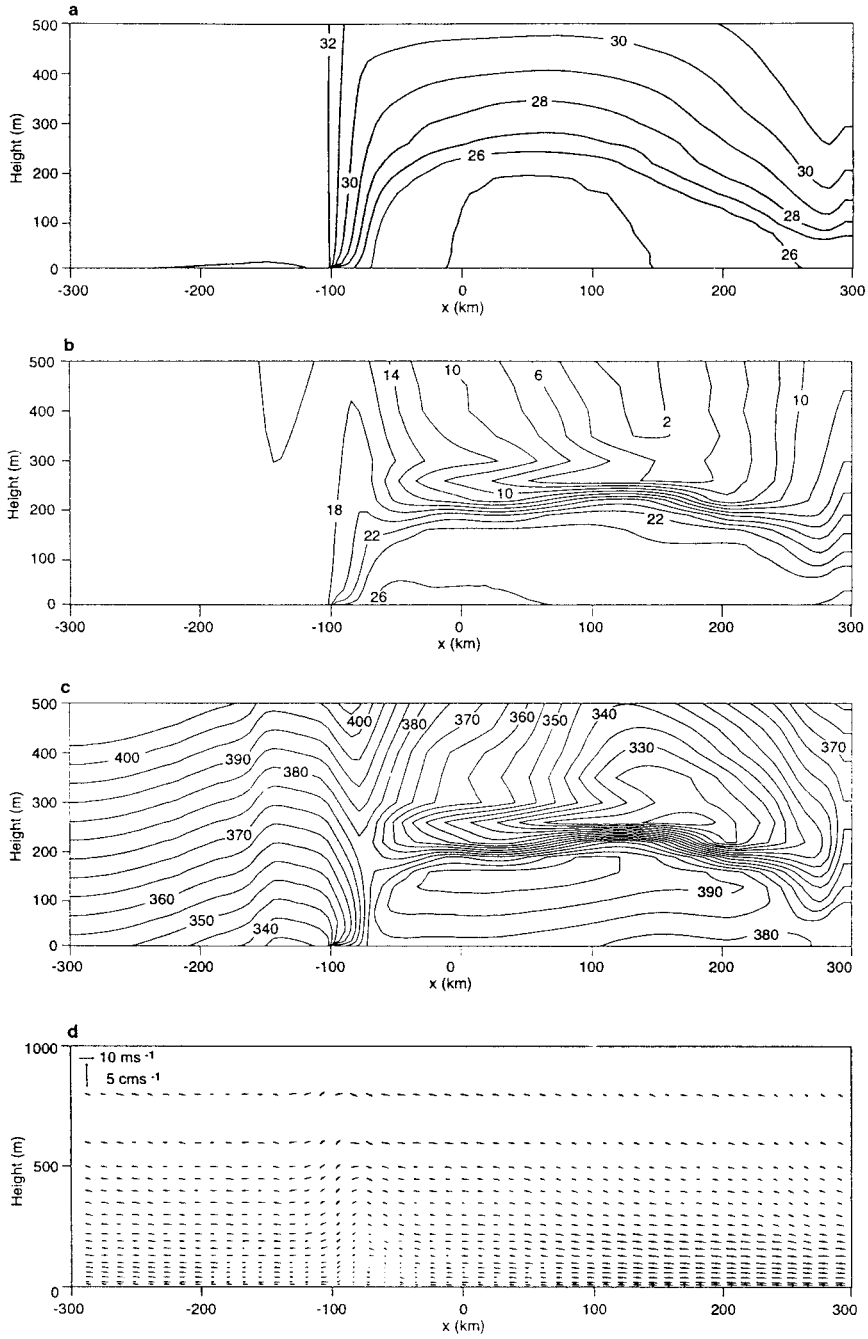

FIG. 12. Cross sections along $y = -54$ km in the low-wind case of set 3: Simulations at 1400 LT of (a) potential temperature (°C), (b) humidity (g kg^{-1}), (c) refractivity (M unit), and (d) u–w winds (key to magnitudes at top left).

humidity distribution. A strong refractivity lapse existed across the temperature inversion region because of its intensity and the strong vertical gradient of humidity, but near the coastline the lapse became horizontal across the SBF. The sea-breeze circulation led to accumulation of water vapor within the circulation area and formed a ''hill-like'' structure of refractivity gradient. This structure would act like a lens to radar waves and produce bending of the waves from sea to coastal land or vice versa. Such bending cannot be described by a simple approach that uses only the vertical refractivity gradient and assumes horizontal homogeneity. The horizontal refractivity gradient in the front had a broadly similar structure to that of the vertical gradient at the top of the MIBL but its value was much smaller (~2 M units km^{-1} as opposed to ~1200 M units km^{-1}).

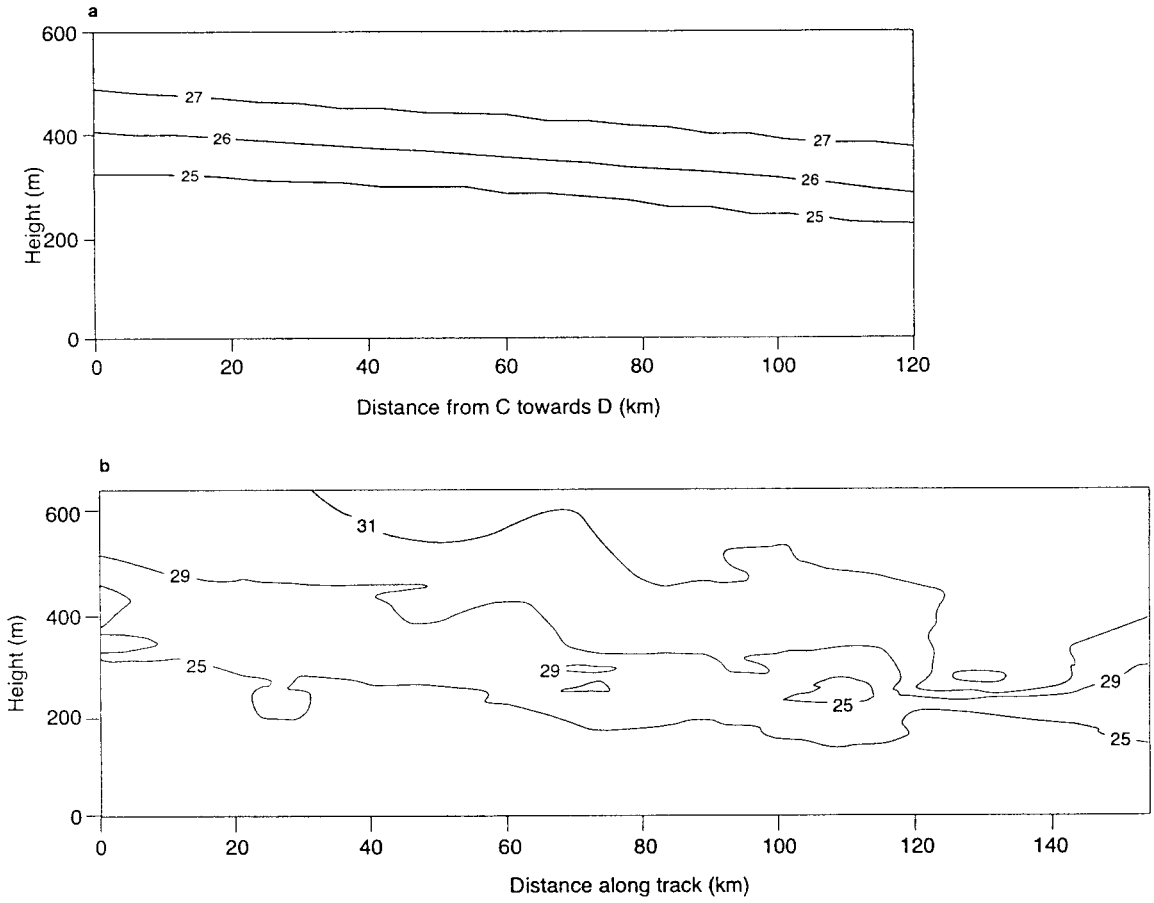

FIG. 13. Cross sections of potential temperature (°C) along line CD in Fig. 2 in the high-wind case of set 3: (a) simulated values at 1400 LT and (b) observations taken in SHAREM-115 on 28 Apr 1996.

2) HIGH-WIND CASE

Figures 13 and 14 show sections of the simulated and observed potential temperature and refractivity along the line CD in Fig. 2. Comparison of the potential temperature sections (Fig. 13) reveals three main points. First, the model captured the inversion capping the MIBL. Second, the downwind slope of the inversion was modeled. Third, the base of the inversion (shown most clearly by the 25°C isoline) and thus the depth of the MIBL were well modeled, but the intensity of the inversion, as noted earlier, was underpredicted. Refractivity was overpredicted by a few percent, and its simulated distribution was out of phase with the pattern seen in the observations (Fig. 14). The simulated high values between 200 and 400 m extend too far downwind, displacing the lower values in the same layer to beyond 80 km. The relatively high values below 200 m and above 500 m are evident in the simulation. The small-scale structures found in both sets of observations were not captured by the simulation, probably for the reasons outlined in section 3d(1) above.

The long section of the high-wind case revealed the same basic structures as those in the low-wind case but with different configurations. The capping inversion was weaker than that in the low-wind case by a factor of about 2 (Fig. 15a). The SBF was more diffuse, having a horizontal temperature gradient about one-half the magnitude of that found in the low-wind case. The slope of the front seen in Fig. 15a has long been recognized as a distinctive facet of the development of sea breezes in opposing ambient wind. Similarly, the front's location offshore in such conditions (Fig. 15d) is a well-documented phenomenon (Atkinson 1981). The effects of the strong ambient wind were also clear in the humidity distribution (Fig. 15b), the marine layer being deeper than in the low-wind case but being bounded by weaker horizontal and vertical gradients. The distribution of refractivity (Fig. 15c) showed a TL varying in height, depth, and intensity over the Gulf. Immediately downwind of the coast, a shallow, simple surface duct occurred within the strong horizontal gradients found there. At larger fetches (say, near $x = 0$ km) it was unclear whether the duct found was an S-shaped surface type or an elevated type. This difficulty in distinguishing between duct types when using a mesoscale model was recognized by Burk and Thompson (1995). At $x = 40$

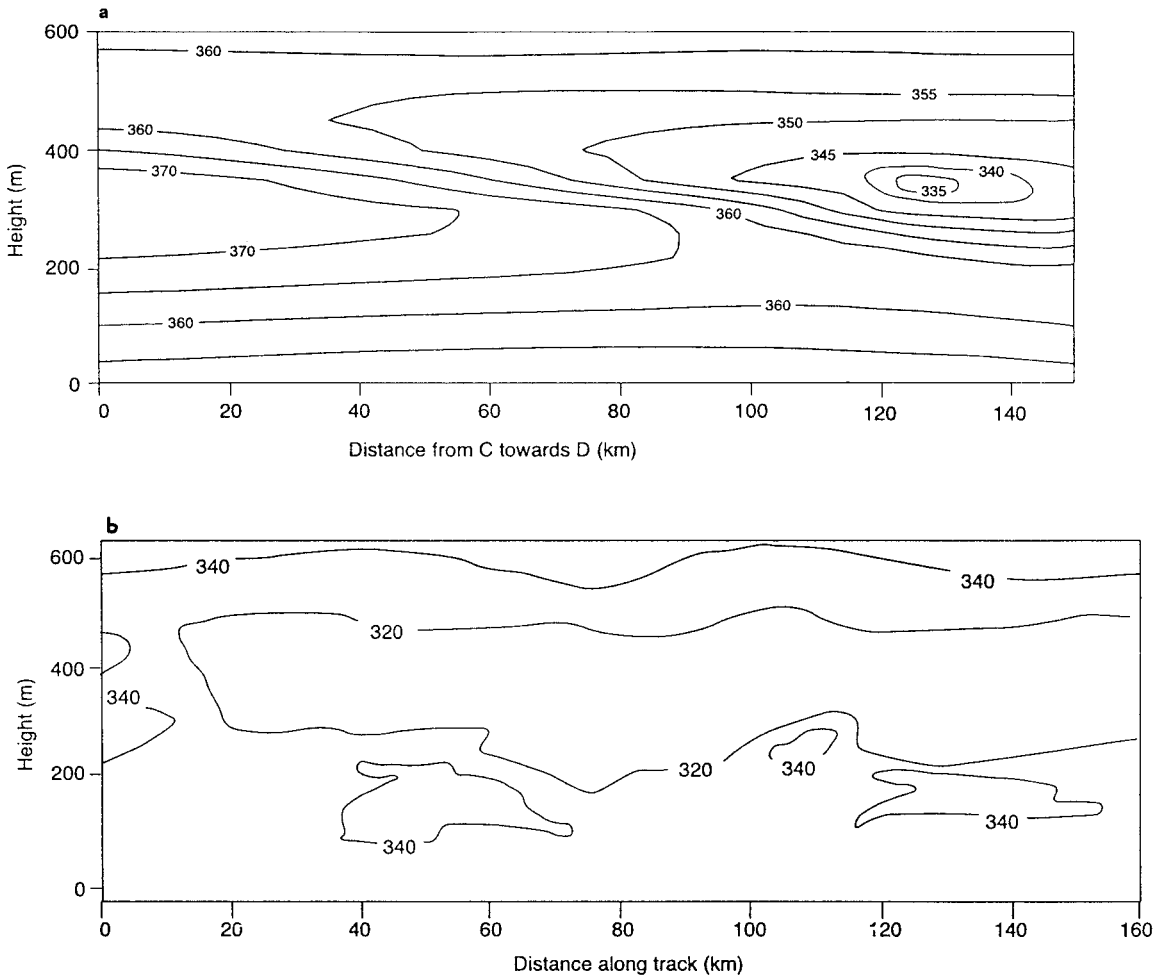

FIG. 14. Cross sections of refractivity (*M* unit) along line CD in Fig. 2 in the high-wind case of set 3: (a) simulated values at 1400 LT and (b) observations taken in SHAREM-115 on 28 Apr 1996.

km, a weak TL lay between 200 and 400 m, giving an S-shaped surface duct beneath 400 m. Yet further downwind, at $x = 200$ km, the TL became stronger and lay between 200 and 300 m. Both the vertical gradient of *M* in the MIBL and the horizontal gradient at the coast were smaller than those in the low-wind case. The observations (I. M. Brooks 1999, personal communication) confirmed the existence of a marine layer that was deeper and bounded by weaker gradients than in the low-wind case.

4. Discussion

The application of a numerical model can cover a wide range of objectives. It is arguable that at one extreme lies simulation, aiming to produce generic information, while at the other lies forecasting, aiming to predict configurations for specific times and places. Between these extremes much scope exists for studies containing aspects of both idealization and realism. To some extent, the kind of modeling is determined by the quality and quantity of data available for initialization and verification. Simulation may be successful with highly idealized initial conditions, whereas good forecasting requires large quantities of high-quality data.

This study was fortunate to have the use of high-quality data on the duct environment in the Persian Gulf, but their quantity and distribution in time and space, together with the relative sparsity of routinely available meteorological data, meant that some idealization was necessary. This was most evident in set 1, which used idealized conditions to represent the marine atmosphere at the time of the SHAREM-115 flights. This group of experiments tested the feasibility of using the model to study the propagation environment in the Gulf. The model was able to capture successfully the different boundary layers over land and sea and, within the latter, to distinguish the states formed under low- and high-wind conditions. A credible mixed boundary layer was generated over land, and conditions over the Gulf waters were found to vary with position and time in a realistic fashion (for example, the SBC).

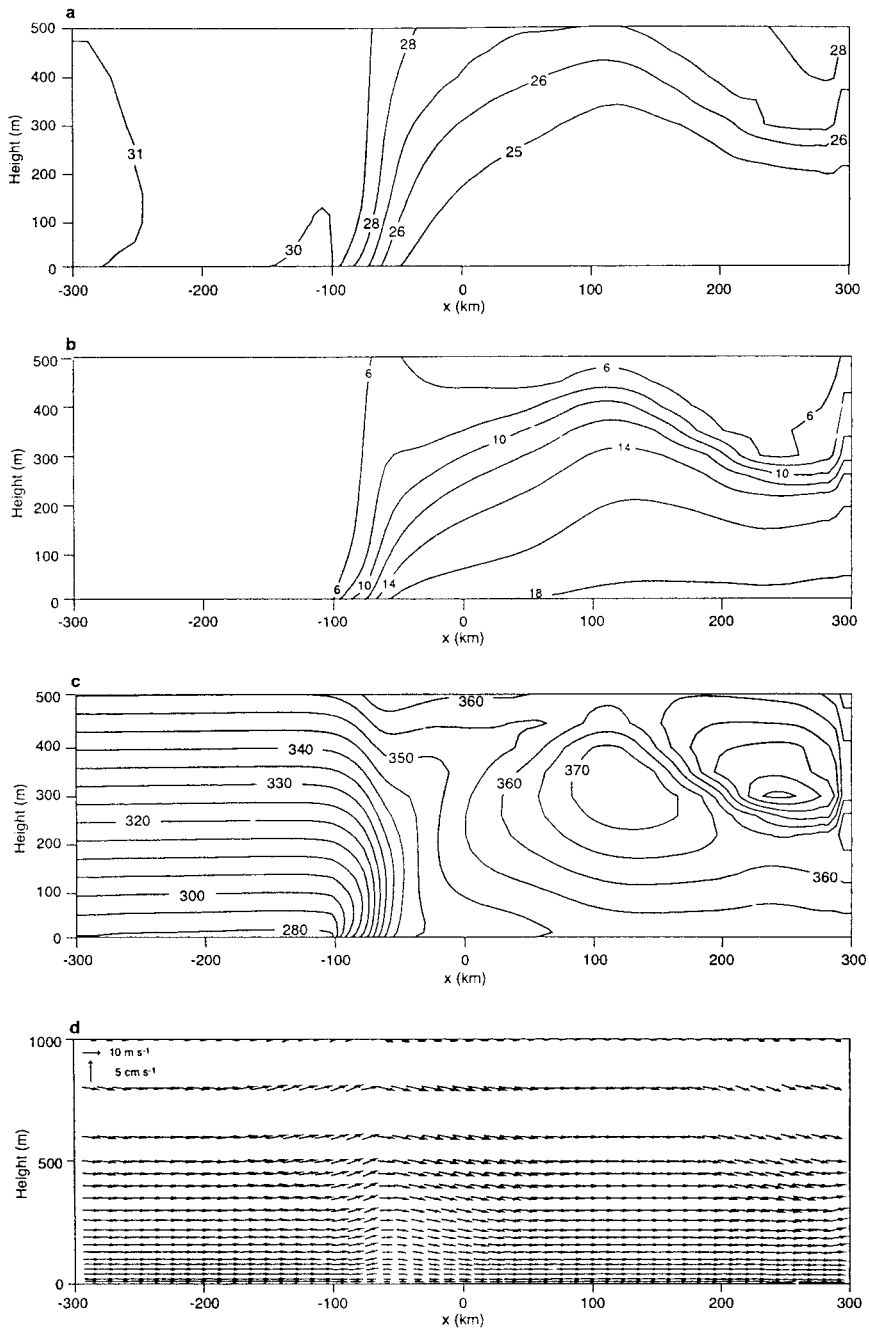

FIG. 15. Cross sections along $y = -54$ km in the high-wind case of set 3: Simulations at 1400 LT of (a) potential temperature (°C), (b) humidity (g kg^{-1}), (c) refractivity (M unit), and (d) u–w winds (key to magnitudes at top left).

Set 2 used less-idealized initial conditions, but, apart from surface values, these conditions were taken from observations over land and so took no account of the distinctive boundary layer over the sea. The initialization was done from one routine ascent several hundred kilometers upwind of the verifying data, and horizontal homogeneity was assumed at all levels except the surface. An MIBL, within which ducts were evident, was produced in both high- and low-wind cases. However, the depths of the ducts were too large and the gradients at the top of the MIBL were underestimated. The use of a single routine land ascent to initialize the model for prediction of duct occurrence, depth, and strength is clearly very attractive. The results of set 2 suggest

that good qualitative information could be obtained in this manner but that for detailed, quantitative prediction such a strategy would be overambitious.

The experiments in set 3 relaxed the assumption of horizontal homogeneity in the initial conditions, using different initial profiles over land and sea. The crucial difference from set 2 is that these runs included an MBL in the initialization. The SHAREM-115 observations gave a description of atmospheric conditions up to a height of 1 km and were used for the sea area in the domain. Above that height, data from a routine ascent was used, and the same ascent was used to describe conditions over the land areas. The results showed distinct improvements over those of set 2. The afternoon MIBLs in both high- and low-wind conditions were in closer agreement with observations than the equivalent cases in set 2. Consequently, the model descriptions of the ducts were much improved. These results show that some knowledge of the near-surface atmosphere over the Gulf water significantly aids the modeling of the existence, depth, and intensity of ducts in that area.

The SHAREM-115 observations revealed structures over the Gulf water on two scales. First, an MIBL was clearly evident, extending over the whole length of the aircraft traverses (over 100 km) and being at most a few hundred meters in depth. The mean MIBL depth in the high-wind cases was about 2 times that in the low-wind cases. The MIBL resulted from the downwind modification of the near-surface atmosphere by the underlying sea surface, giving rise to distinctive profiles of temperature, stability, and humidity. In turn, these profiles affected the profiles of refractivity. Second, within the MIBL lay smaller structures, measuring a few kilometers in the horizontal and a few tens of meters in the vertical. The origins of these structures are uncertain but are likely to be related to at least two factors. First, because the heat flux at the sea surface provides a forcing mechanism for MIBL development it is possible that inhomogeneity in the SST on the appropriate scale influenced the fine structure of the MIBL. Second, the shape and height of the fine structures suggests that mixing at the top of the MIBL could be a significant mechanism. The small-scale structures were not seen in the simulations. The uniform SST used in these experiments could be a partial explanation for this. The small scale of the structures relative to the model grid length could also be an important factor, and it was therefore not surprising that the fine structure was missing from the results.

In contrast, the MIBL per se was well simulated. The moist, cool, stable layer that results when air flows from warmer land over cooler sea was clearly evident in the results. It was bounded by strong vertical gradients at the top of the layer and by their equivalents in the horizontal at its landward limit. Because it is also forced by land–sea contrasts, the sea-breeze circulation, a substantially documented phenomenon (Atkinson 1981), frequently occurs in association with the MIBL. The size, location, and internal structure of the sea-breeze circulation were realistically simulated. The gradients of temperature and humidity that bound the MIBL cause perturbations in the refractivity distribution that, in turn, lead to TLs and ducts. The existence, location, and surface character of the ducts were well captured. Horizontal variations in duct characteristics due to the SBC were elucidated. The simulations successfully distinguished between high- and low-wind occasions, a notable feature of the SHAREM-115 observations. The modeled magnitudes of duct depth and strength, although leaving scope for improvement, were most encouraging.

5. Conclusions

The vertical structure of the ABL, particularly strong gradients at the top of the layer, can significantly affect the propagation of electromagnetic waves. For example, it may produce ducting of radar waves. A three-dimensional, time-dependent, nonhydrostatic numerical model was used to simulate the atmosphere over the Persian Gulf in which significant ducting occurred on the occasion of aircraft observations in that area. The observations had been divided into high- and low-wind cases, and the same framework was used for the simulations reported here.

Three sets of experiments were conducted with initial conditions of varying degrees of idealization. All three produced results in agreement with the observations taken in the SHAREM-115 program, but the level of agreement was sensitive to the initial conditions. The best results were obtained when the initialization explicitly included data on the MBL gathered by the aircraft program. The simulations showed the development of MIBLs in air flowing from the desert lands west of the Persian Gulf over the waters of the Gulf itself. The MIBLs were capped by temperature inversions that were associated with lapses of humidity and refractivity. As compared with the high-wind case, the low-wind MIBL was shallower and the gradients at its top were sharper. The model successfully captured the existence of surface ducts in both high- and low-wind conditions, but their depths tended to be overestimated and their strengths underestimated. In addition, the simulations revealed a sea-breeze circulation that accorded well with previous knowledge of that feature. In the low-wind case, the forward edge of the sea air resembled a broad SBF. The interplay of opposing ambient wind and the sea breeze itself resulted in the front being virtually stationary near the coastline. In the high-wind case, the front was less intense and lay somewhat downwind of the coast, a result of the stronger opposing ambient wind. Horizontal gradients of temperature, humidity, and refractivity associated with the ‘‘fronts’’ in the sea-breeze circulations were linked to the vertical gradients at the top of the MIBLs. These horizontal variations complement those on a smaller scale revealed by ob-

servations (Brooks et al. 1999) and emphasize the need to incorporate horizontal heterogeneity into the analysis and prediction of the propagation environment.

Acknowledgments. The authors are grateful to the Meteorological Support Group of the U.K. Ministry of Defence for financial support of this research project. We also thank Mr. E. Oliver for drawing the diagrams.

REFERENCES

André, J. C., and L. Mahrt, 1982: The nocturnal surface inversion and influence of clear-air radiative cooling. *J. Atmos. Sci.,* **39,** 864–878.

Arritt, R. W., 1993: Effects of the large-scale flow on characteristic features of the sea breeze. *J. Appl. Meteor.,* **32,** 116–125.

Atkinson, B. W., 1981: *Mesoscale Atmospheric Circulations.* Academic Press, 495 pp.

——, 1995: Orographic and stability effects on valley-side drainage flows. *Bound.-Layer Meteor.,* **75,** 403–428.

——, and A. N. Shahub, 1994: Orographic and stability effects on day-time, valley-side slope flows. *Bound.-Layer Meteor.,* **68,** 275–300.

Babin, S. M., 1995: A case study of subrefractive conditions at Wallops Island, Virginia. *J. Appl. Meteor.,* **34,** 1028–1038.

——, 1996: Surface duct height distributions for Wallops Island, 1985–1994. *J. Appl. Meteor.,* **35,** 86–93.

——, and J. R. Rowland, 1992: Observation of a strong surface radar duct using helicopter acquired fine-scale radio refractivity measurements. *Geophys. Res. Lett.,* **19,** 917–920.

——, G. S. Young, and J. A. Carton, 1997: A new model for the oceanic evaporation duct. *J. Appl. Meteor.,* **36,** 193–204.

Ballard, S. P., B. W. Golding, and R. N. B. Smith, 1991: Mesoscale model experimental forecasts of the Haar of northeast Scotland. *Mon. Wea. Rev.,* **119,** 2107–2123.

Barrios, A. E., 1995: Terrain and refractivity effects in a coastal environment. *Conf. on Propagation Assessment in Coastal Environment,* Bremerhaven, Germany, AGARD/NATO, 9.1–9.5.

Bean, B. R., and E. J. Dutton, 1968: *Radio Meteorology*. Dover, 435 pp.

Bechtold, P., J.-P. Pinty, and P. Mascart, 1991: A numerical investigation of the influence of large-scale winds on sea-breeze- and inland-breeze-type circulations. *J. Appl. Meteor.,* **30,** 1268–1279.

Brooks, I. M., and D. P. Rogers, 2000: Aircraft observations of the mean and turbulent structure of a shallow boundary layer over the Persian Gulf. *Bound.-Layer Meteor.,* **95,** 189–210.

——, A. K. Goroch, and D. P. Rogers, 1999: Observations of strong surface radar ducts over the Persian Gulf. *J. Appl. Meteor.,* **38,** 1293–1310.

Burk, S. D., and W. T. Thompson, 1995: Mesoscale modeling of refractive conditions in a complex coastal environment. *Conf. on Propagation Assessment in Coastal Environment,* Bremerhaven, Germany, AGARD/NATO, 40.1–40.7.

——, and ——, 1997: Mesoscale modeling of summertime refractive conditions in the Southern California Bight. *J. Appl. Meteor.,* **36,** 23–31.

Carpenter, K. M., 1979: An experimental forecast using a non-hydrostatic mesoscale model. *Quart. J. Roy. Meteor. Soc.,* **105,** 629–656.

Christophe, F., N. Douchin, Y. Hurtaud, D. Dion, R. Makaruschka, H. Heemskert, and K. Anderson, 1995: Overview of NATO/AC 243/Panel 3 activities concerning radio wave propagation in coastal environments. *Conf. on Propagation Assessment in Coastal Environment,* Bremerhaven, Germany, AGARD/NATO, 27.1–27.9.

Cook, J., G. Vogel, and G. Love, 1995: Operational support for a range-dependent radio propagation model. *Conf. on Propagation Assessment in Coastal Environment,* Bremerhaven, Germany, AGARD/NATO, 13.1–13.7.

Craig, K. H., 1988: Propagation modelling in the troposphere: Parabolic equation method. *Electr. Lett.,* **24,** 1136–1139.

——, and T. G. Hayton, 1995: Climatic mapping of refractivity parameters from radiosonde data. *Conf. on Propagation Assessment in Coastal Environment,* Bremerhaven, Germany, AGARD/NATO, 43.1–43.12.

Dare, R. A., and B. W. Atkinson, 1999: Numerical modeling of atmospheric response to polynyas in the Southern Ocean sea ice zone. *J. Geophys. Res.,* **104,** 16 691–16 708.

Dockery, G. D., and J. Goldhirsh, 1995: Atmospheric data resolution requirements for propagation assessment: Case studies of range-dependent coastal environments. *Conf. on Propagation Assessment in Coastal Environment,* Bremerhaven, Germany, AGARD/NATO, 7.1–7.12.

Finkele, K., J. M. Hacker, H. Kraus, and R. A. D. Byron-Scott, 1995: A complete sea-breeze circulation cell derived from aircraft observations. *Bound.-Layer Meteor.,* **73,** 299–317.

Garratt, J. R., 1990: The internal boundary layer—a review. *Bound.-Layer Meteor.,* **50,** 171–203.

——, and B. F. Ryan, 1989: The structure of the stably stratified internal boundary layer in offshore flow over the sea. *Bound.-Layer Meteor.,* **47,** 17–40.

Golding, B. W., 1987: The U.K. Meteorological Office mesoscale model. *Bound.-Layer Meteor.,* **41,** 91–107.

——, 1990: The Meteorological Office mesoscale model. *Meteor. Mag.,* **119,** 81–96.

Levy, M. F., 1995: Fast PE models for mixed environments. *Conf. on Propagation Assessment in Coastal Environment,* Bremerhaven, Germany, AGARD/NATO, 8.1–8.6.

——, and K. H. Craig, 1992: Use of mesoscale models for refractivity forecasting. *Conf. on Remote Sensing of the Propagation Environment,* Cesme, Turkey, AGARD/NATO, 7.1–7.11.

Li, J.-G., and B. W. Atkinson, 1999: Transition regimes in valley airflows. *Bound.-Layer Meteor.,* **91,** 385–411.

Lystad, S., and T. Tjelta, 1995: High-resolution meteorological grid for clear air propagation modelling in northern coastal regions. *Conf. on Propagation Assessment in Coastal Environment,* Bremerhaven, Germany, AGARD/NATO, 41.1–41.12.

Rogers, D. P., D. W. Johnson, and C. A. Friehe, 1995: The stable internal boundary layer over a coastal sea. Part I: Airborne measurements of the mean and turbulence structure. *J. Atmos. Sci.,* **52,** 667–683.

Rogers, L. T., 1995: Effects of spatial and temporal variability of atmospheric refractivity on the accuracy of propagation assessments. *Conf. on Propagation Assessment in Coastal Environment,* Bremerhaven, Germany, AGARD/NATO, 31.1–31.9.

Tapp, M. C., and P. W. White, 1976: A non-hydrostatic mesoscale model. *Quart. J. Roy. Meteor. Soc.,* **102,** 277–296.

Turton, J. D., D. A. Bennetts, and S. F. G. Farmer, 1988: An introduction to radio ducting. *Meteor. Mag.* **117,** 245–254.

Wu, J., 1982: Wind stress coefficients over sea surface from breeze to hurricane. *J. Geophys. Res.* **87,** 277–296.